Crustal structure of the Borderland-Continent Transition Zone of southern California adjacent to Los Angeles

Julie J. Nazareth and Robert W. Clayton

Seismological Laboratory, California Institute of Technology, Pasadena, California, USA

Received 31 July 2000; revised 16 May 2002; accepted 11 February 2003; published 30 August 2003.

[1] We use data from the onshore-offshore component of Los Angeles Region Seismic Experiment (LARSE) to model the broad-scale features of the midcrust to upper mantle beneath a north-south transect that spans the continental borderland in the Los Angeles, California, region. We have developed an analysis method for wide-angle seismic data that consists primarily of refractions, lacks near-offset recordings, and contains wide gaps in coverage. Although the data restrict the analysis to the modeling of broad-scale structure, the technique allows one to explore the limits of the data and determine the resolving power of the data set. The resulting composite velocity model constrains the crustal thickness and location and width of the continent-Borderland transition zone. We find that the mid to lower crust layer velocities of the Inner Borderland are slightly lower than the corresponding layers in the average southern California crust model, while the upper mantle velocity is significantly higher. The data require the Moho to deepen significantly to the north. We constrain the transition zone to initiate between the offshore slope and the southwest Los Angeles Basin. If the Inner Borderland crust is 22 km thick, then the transition zone is constrained to initiate within a 2 km wide region beneath the southwest Los Angeles Basin, and have a width of 20–25 km. The strong, coherent, and continuous *Pn* phase suggests the Moho is coherent and laterally continuous beneath the Inner Borderland and transition zone. The Inner California Borderland seems to be modified and thickened oceanic crust, with the oceanic upper mantle intact beneath it. *INDEX TERMS:* 0935 Exploration Geophysics: Seismic methods (3025); 8105 Tectonophysics: Continental margins and sedimentary basins (1212); 0902 Exploration Geophysics: Computational methods, seismic; 7205 Seismology: Continental crust (1242); 7220 Seismology: Oceanic crust; *KEYWORDS:* California Borderland, LARSE, transition zone, slab

Citation: Nazareth, J. J., and R. W. Clayton, Crustal structure of the Borderland-Continent Transition Zone of southern California adjacent to Los Angeles, *J. Geophys. Res.*, *108*(B8), 2404, doi:10.1029/2001JB000223, 2003.

1. Introduction

[2] The western margin of the North America plate is an area of active deformation that is in part related to its past subduction history. Although subduction has ceased off the coast of most of California, the subduction legacy on the continent remains in the crustal structure and rocks of the great batholiths, sedimentary basins, and metamorphic complexes. Recent seismic experiments (summarized by *Fuis* [1998]) along the western margin of North America reveal that historical remnants of subduction (usually underplated fragments of oceanic plates and/or magmatic underplating) can exist and is in fact quite common in the mid to lower crust without obvious surficial expression on the continent. In southern California, subduction of the very young and fragmented Farallon plate terminated approximately 28 Ma as the Pacific-Farallon ridge intersected the Farallon-North America trench [*Atwater*, 1989]. The fate of the slab or slab fragments in this region is unknown [*Atwater and Stock*, 1998].

[3] The Los Angeles Region Seismic Experiment (LARSE) is a multiphase, multicomponent study of the crustal structure of southern California carried out by the Southern California Earthquake Center and the U.S. Geological Survey [*Fuis et al.*, 1996]. LARSE includes a passive seismic survey [*Kohler et al.*, 1996], deep crustal reflection and refraction surveys from onshore and offshore sources with onshore and ocean-bottom seismometers, and an offshore multichannel seismic survey [*Brocher et al.*, 1995; *Okaya et al.*, 1996; *ten Brink et al.*, 1996]. In this paper, data from the onshore-offshore component of LARSE are analyzed.

[4] The onshore-offshore component of LARSE is a wide-angle reflection/refraction experiment designed to investigate the mid to lower crustal structure in the nearshore California Continental Borderland and the adjacent continental region. The crustal structure and features of the interface between the oceanic crust and the continental crust in the Borderland region are not well known but have important implications for both the tectonic history and

0148-0227/03/2001JB000223$09.00

current tectonics of the Borderland and the greater Los Angeles region. This analysis also provides a link between on-land and marine models of crustal structure in southern California.

[5] The onshore-offshore portion of LARSE (Figure 1) crossed four tectonic regions: the (offshore) Inner California Borderland, the Los Angeles basin, the central Transverse Ranges, and the Mojave Desert. Because of the wide-angle nature of the experiment, the area of significance in interpretation of the data is the offshore Borderland and onshore Los Angeles Basin.

[6] The California Borderland structural province is characterized by northwest trending ridges separated by broad, flat basins [*Shepard and Emery*, 1941; *Emery*, 1954]. Extensional basins formed during Miocene to Pliocene time [*Bohannon and Geist*, 1998], and were accentuated by a structural inversion to northeast-southwest compression since early Pliocene [*Crouch and Suppe*, 1993]. Most basins contain 2–5 km of sediment, which is a significant portion of the 20–27 km thickness of the Borderland crust [*Couch and Riddihough*, 1989; *Mooney and Weaver*, 1989; *Bohannon and Geist*, 1998]. Recent studies in the region of the LARSE profiles find a crustal thickness of 19–23 km in the area between Santa Catalina Island and the coastline to the north and northeast [*Richards-Dinger and Shearer*, 1997; *Hauksson*, 2000; *Zhu and Kanamori*, 2000; *ten Brink et al.*, 2000]. The Borderland consists of four main lithostratigraphic belts that divide the structural province into the Inner California Borderland (Catalina Schist belt), the Outer California Borderland (Patton accretionary belt and Nicholas forearc belt), and the western Transverse Ranges block (western Transverse Ranges belt) [*Crouch and Suppe*, 1993; *Bohannon and Geist*, 1998]. High *P* wave velocities of 6.7 to 7.2 km/s in the mid to lower crust imply an oceanic origin for the crust in this region [*Mooney and Weaver*, 1989].

[7] Located at the intersection of the Peninsular Ranges, the Transverse Ranges, and the California Borderland, the Los Angeles basin is a small but deep basin with thick, mainly Neogene sedimentary fill [*Yerkes et al.*, 1965; *Wright*, 1991]. The 8 km thick basin is underlain by high-velocity material [*Hauksson and Haase*, 1997; *Hauksson*, 2000] that may be related to the formation of the ancestral basin in the middle Miocene from block rotations [*Luyendyk et al.*, 1980] or rifting [*Crouch and Suppe*, 1993]. Crustal thickness transitions rapidly beneath the Los Angeles basin from the ~20 km of the Inner Borderland to ~30 km beneath the Transverse Ranges [*Zhu and Kanamori*, 2000].

[8] The late Cenozoic, east-west trending Transverse Ranges trend across the coast parallel orientation of tectonic features along the western margin of North America. The Transverse Ranges are composed of a series of parallel to sub-parallel ranges and intervening valleys, including the San Gabriel, Santa Monica, and Santa Susanna Mountains, and the intervening San Fernando and San Gabriel valleys in the central portion of the ranges. Uplift of the Transverse Ranges has been attributed to the left stepping bend in the right lateral San Andreas fault and clockwise block rotation during the Miocene [*Ehlig*, 1981]. Crustal thickness beneath the central Transverse Ranges is estimated to be approximately 29 km from teleseismic receiver function modeling [*Zhu and Kanamori*, 2000], *Pn* travel time modeling [*Hearn and Clayton*, 1986; *Sung and Jackson*, 1992], and from stacking short-period *PmP* phases [*Richards-Dinger and Shearer*, 1997]. *Kohler and Davis* [1997] inferred a 40 km thick crust beneath the San Gabriel Mountains from teleseismic travel time residuals. The San Gabriel Mountains form a high-velocity ridge down to at least 20 km depth with velocities as high as 5–6.3 km/s at 1 km depth [*Hauksson and Haase*, 1997; *Hauksson*, 2000].

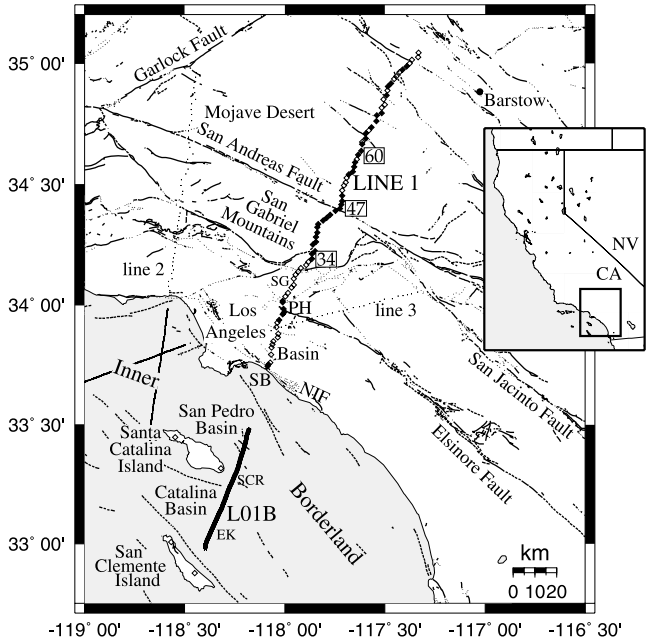

Figure 1. Location of LARSE experiment. Ship track L01B (air gun positions) is marked by a thick line. Receivers are marked with diamonds, with filled diamonds showing stations used in this analysis. The numbers identify the location of stations 34, 47, and 60. Lines 2 and 3 (not analyzed in this paper) are marked by thin lines offshore changing to dots onshore (receiver locations). Solid, dashed, and dotted lines represent faults. EK, Emery Knoll; NIF, Newport-Inglewood Fault; PH, Puente Hills; SB, Seal Beach; SCR, Santa Catalina Ridge; SG, San Gabriel Valley. In the small plot, thin lines mark state boundaries and the box outlines the area of the large map. CA, California; NV, Nevada.

[9] At the far end of the profiles, the Mojave Desert is a broad elevated region of low mountains of Mesozoic igneous rocks and basins with Cenozoic sediments. Elevations of much of the region lie between 600 and 1200 m. The province is approximately bounded by the San Andreas fault to the south and the Garlock fault to the north, with indistinct eastern and southeastern boundaries. Crustal thickness is estimated to be 29–30 km with a flat Moho [*Richards-Dinger and Shearer*, 1997; *Zhu and Kanamori*, 2000].

2. Experiment Description

[10] The onshore-offshore portion of LARSE consists of 22,128 air gun shots and 172 on-land vertical seismometers along three profiles in the greater Los Angeles area (Figure 1). Energy from the 139 L air gun array, towed by the R/V

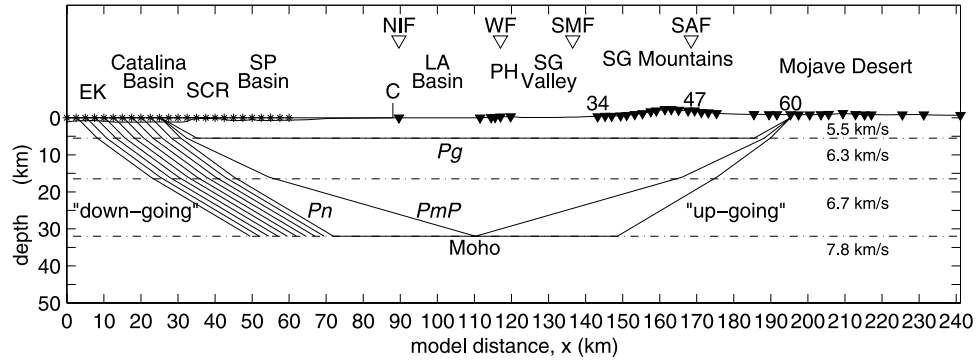

Figure 2. Source-receiver geometry in cross section. There are gaps at the surface, but throughgoing rays at depth. The limited range covered and the gaps in coverage restrict the analysis to simple layered models. Velocities and depths shown are for the average southern California crust model [*Wald et al.*, 1995]. Stars mark the approximate extent of the offshore sources for LARSE ship track L01B. On-land receivers with usable (though sometimes poor quality) data are marked by inverted triangles. Receivers 34, 47, and 60 are identified by numbers. C, the coast; EK, Emery Knoll; LA Basin, Los Angeles Basin; NIF, Newport-Inglewood Fault; PH, Puente Hills; SAF, San Andreas Fault; SCR, Santa Catalina Ridge; SG Valley, San Gabriel Valley; SG Mountains; San Gabriel Mountains; SMF, Sierra Madre Fault; SP Basin, San Pedro Basin; WF, Whittier Fault.

Ewing, was recorded over 230 km away in the Mojave Desert. Air gun sources were spaced 50 m apart on average, and the land receivers were nominally spaced 2 km apart. This paper analyzes the southwest-northeast oriented profile shot during the experiment (line 1).

[11] Line 1 extends from San Clemente Island to the Mojave Desert northwest of Barstow. We analyzed ship track L01B (Figure 1), which consists of 1307 shots with source-receiver offsets between 30 and 241 km. Of 82 possible receivers, 38 provided adequate quality data for the analysis. Data quality was good for receivers located in the San Gabriel Mountains and on San Clemente and Santa Catalina Islands, moderate to poor in the Mojave Desert, and generally poor along the coast and in the Los Angeles basin. Two stations located in the Puente Hills provide moderate quality data for the general Los Angeles basin region. Poor quality and nonfunctioning stations produced several large data gaps in the Los Angeles basin and San Gabriel Valleys. Basins tend to trap cultural noise and deflect external seismic energy incident from below, producing recordings with low signal-to-noise ratios. Head wave phases traveling to the San Gabriel Mountain stations travel beneath the basin before turning up to the surface and are thus not affected.

[12] Figure 2 shows the geometry of the experiment in cross section. There is a gap between the air gun sources and the receivers on land; however, the rays sample the structure of the ocean-continent transition at midcrustal to upper mantle depths. Additional gaps are due to poor quality or nonexistent data, such as for the Los Angeles basin. These gaps affect mostly the interpretation of the upper crust, which is not the focus of this paper.

3. Technique

[13] We have developed an analysis method for wide-angle seismic data that consists primarily of refractions (rays that travel mostly horizontal through the crust), lacks near-offset recordings, and contains wide gaps in coverage. The geometry of the ray paths do not allow for travel time inversion because of the lack of crossing rays. Therefore the data restrict the analysis to the investigation and modeling of somewhat simple, broad-scale structure, that is best represented by layered velocity models. However, the technique allows one to explore the limits of the data to find a suite of models that fit the data and illustrate the resolving power of the data set.

[14] We demonstrate the technique assuming the standard source-receiver geometry of an onshore-offshore seismic experiment (Figure 2). The air gun sources offshore are spaced close together and the number of sources exceed by far the more sparsely spaced receivers onshore. There is a gap at the surface between the sources and receivers, but the seismic rays are throughgoing at mid to lower crustal depths. For this experiment geometry, the seismic data are best viewed as receiver gathers because of the numerous closely spaced sources.

[15] The analysis technique consists of six main steps: (1) remove the upper crustal near-source effects (for receiver gathers); (2) separate the phases and estimate the apparent velocities and intercept times through a Radon transform; (3) pick the phases; (4) identify any trends in the picks; (5) remove the upper crustal near-receiver effects through station delays; and (6) construct a suite of velocity models that fit the constraints of the data.

3.1. Removing the Effects of Near-Source Structure

[16] In an onshore-offshore experiment that recorded primarily refractions or head waves, the only upper crustal regions that affect the data are directly beneath the source region at sea (the downgoing paths from the sources), and the "single" upgoing path to each receiver (Figure 2). For each type of head wave (e.g., *Pn*, *Pg*, or other unnamed) there is a single downgoing path for its source and a single upgoing path for the receiver. Consequently, these shallow regions beneath the sources only manifest themselves as static corrections to the data set that are largely offset independent. We remove the effects of these shallow

regions by empirically estimating a static correction for each source point in the survey.

[17] The procedure we have adopted is to account for as much of the upper crustal structure as possible with the static corrections. We first account for the upper crustal effects from beneath the sources with a static source correction that can be applied to all receiver gathers. The variations that remain between the receiver gathers will be used to determine the structure beneath and between the sources and receivers. This approach will tend to produce the simplest structure that is consistent with the data. The resulting model will also be consistent with the OBS and on-land explosion data, since they provide very little constraint on the near vertical travel time from the mid and lower crust.

[18] To correct the data for the near-source effects, we use a first arrival refraction (head wave) as the guide (pilot) for the correction. The phase chosen as the pilot for the correction should be the strongest arrival over most of the source-receiver offsets and the first arrival at most if not all of the offsets for the model receiver gather. The onset of the head wave is picked, and each trace is linearly shifted along the time axis to align the arrival at the proper apparent velocity across the entire model receiver gather. We pick the arrival times of the head wave by cross correlating with a representative wavelet chosen from the gather. Obvious cycle skips due to the reverberative nature of the data are edited by hand. Some traces are eliminated because of bad waveforms, apparent cycle skips, and noise. This has a minimal affect the analysis because the discarded traces are usually distributed throughout the receiver gather and represent a relatively small portion of the total data volume. We remove the mean of the time shifts, so that a constant time shift is not added to the data. This static correction is then applied to every receiver gather along the profile.

[19] Although the correction is based upon a single phase (usually *Pn*), it works well for all head wave arrivals in the receiver gather because the difference in travel path between the mid and lower crustal head waves is small (less than 5° in water). Midcrustal reflected phases can be treated in the same manner if their move out is approximately linear over the range of offsets in the experiment. *PmP* is not linear at the offsets in most wide-angle experiments. The error in processing the *PmP* phase depends on the curvature in the *PmP* arrival, which in turn depends on the offset range of the experiment and the thickness of the crust. Ray tracing tests show the error for *PmP* at offsets similar to those for the LARSE experiment is on the order of −0.10 to + 0.10 s. These errors will result in slight smearing of the Radon transform, which is discussed in the next section.

[20] The static correction is designed to remove the lateral time variations in a phase due to variations in seafloor depth and basin structure beneath the sources, but does not correct for the average travel time delay due to the seawater. We estimate this average delay from the mean water column correction

$$W = \left(\frac{d}{v_w \cos\alpha}\right) - \left(\frac{d}{v \cos\alpha}\right) \quad (1)$$

where d is the seafloor depth (water column thickness), v_w is the velocity of seawater, v is the velocity of rock used for the upper crust during velocity modeling (step 6), and α is the angle from vertical of the ray path in the seawater. This delay is accounted for during velocity modeling (step 6) by removing the mean water column correction from data intercept times.

[21] Long-wavelength variations can present a problem for static corrections. For example, a systematic dip in the seafloor toward the offshore will make the arrivals appear apparently slower than they really are. If the correct apparent velocity is chosen to align the pilot head wave, then the static correction removes the effect of systematic dip in the seafloor. If, however, a slightly faster or slower apparent velocity is chosen to align the pilot head wave, then the static correction will impart a corresponding shift in apparent velocity to all of the phases in the section (the effect is exact in slowness, but is approximate in velocity). We believe in most cases, the correct apparent velocity of the pilot head wave can be properly estimated to within ±0.1 km/s by comparing the lateral time variations of the pilot head wave to the depth of the seafloor beneath the sources.

3.2. Radon Transform

[22] To estimate apparent velocities and intercept time, we apply a Radon transform to the corrected receiver gather [*Yilmaz*, 1987]:

$$S(p,\tau) = \int P(X, \tau + pX)dX \quad (2)$$

where p is the ray parameter, X is the offset, $\tau = t\text{-}pX$ is the time intercept, and t is the travel time. The Radon transform separates arrivals based on their respective horizontal slownesses and time intercepts. It averages over imperfections in the near-source correction on individual traces and gives the average horizontal slowness and time intercept of the phase, so consequently has the effect of laterally smoothing the velocity structure. This is appropriate since most of the rays in this data set are primarily horizontal (head waves) and hence already average over lateral variations. We apply an envelope function to the transformed data, to help in picking the various phases.

3.3. Pick the Phases

[23] The main interpretive step in this analysis is in picking the phases in the Radon transform. We demonstrate this with a synthetic example. The synthetic travel times from an average southern California crust model [*Wald et al.*, 1995] have been convolved with a representative waveform to simulate the multiple reverberations found in the actual data (Figure 3a). The resulting envelope of the Radon transform is shown in Figure 3b. A full range of source-receiver offsets would result in a series of stacked ellipses as shown by the dotted line in Figure 3b, with the head waves located at the intersection of the ellipses (solid circles), wide-angle reflections along the outside curve, and precritical reflections on the inside curves. However, the range of offsets limits the data to head waves and wide-angle reflections, so we are left with a monotonic curve. Reverberations in the data lead to an elongation of the curve in the τ direction, so head wave points become approximately elliptical with the long axis in the τ direction. The width of the amplitude peak in the τ direction is proportional to the length of the wave train of the arrival.

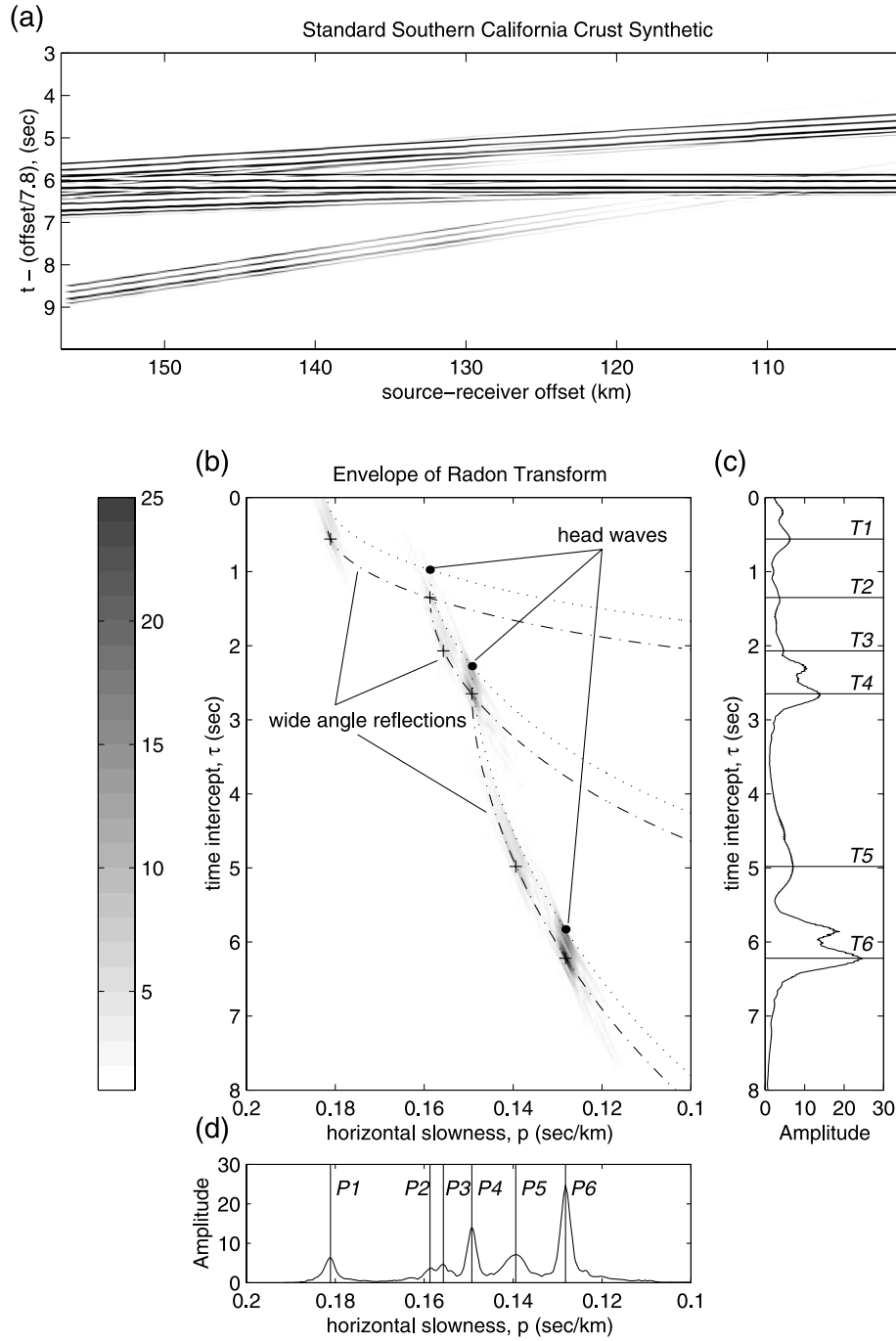

Figure 3. Synthetic example to demonstrate the picking process. (a) Reduced time section based upon the average southern California crust model [*Wald et al.*, 1995]. Convolved with representative waveform to simulate the multiple reverberations found in the LARSE data. (b) Envelope of the Radon transform. Dotted line represents theoretical stacked ellipses of the Radon transform of full offset impulsive arrival data. The dashed line shows the theoretical ellipses delayed by 0.38 s, representing the delay in the waveform from onset to maximum amplitude. (c) Maximum amplitude of each row (time intercept, τ, axis). Peak picks corresponding to the peak picks of 3d, labeled T1–T6. (d) Maximum amplitude of each column (horizontal slowness, p, axis). Peak picks labeled P1–P6, represent the apparent horizontal slowness of the three head wave and three reflection phases.

[24] To simplify picking and increase accuracy, we find the maximum amplitude of each column (i.e., for every value of horizontal slowness, p) and each row (i.e., time intercept, τ). The corresponding curves for our synthetic example are shown in Figures 3c and 3d with numbered lines indicating the location of the picks. We show the picks as crosses on the Radon transform envelope (Figure 3b). The six peaks of varying amplitude in Figure 3d represent

the average horizontal slownesses of the reflected and refracted phases that result from this model. The reflected phases (numbered P1, P3, P5) will have broader peaks along the p axis than the head waves (numbered P2, P4, P6) with the Radon transform. The shallower reflections (numbered P1 and P3) are approximately linear in the time section at the offsets in this model (similar to the offsets found in the LARSE data), so they produce narrow peaks along the p axis. The largest amplitude of every peak corresponds to the time of the maximum amplitude in the wave train of the arrival (a 0.38 s delay for this example), not the onset of the arrival. The relative time differences between the phases are maintained, but the static time shift implies a thicker upper crustal layer. To minimize this effect, we estimate the delay of the peak amplitude within the wave train reverberations and decrease the value of all τ picks by this amount during velocity modeling (step 6).

[25] Radon transforms are computed for each receiver gather and picked individually. All major peaks in amplitude are initially assumed to represent refracted or possibly reflected phases, and their p values are picked from the column maximum curve. The corresponding time intercepts of those p picks are simply the τ values that have the same amplitude as the p pick. Unlike synthetic data, real data contains noise that leads to energy in the radon transform distributed away from a single monotonic curve, causes spurious peaks (and therefore spurious picks), and contributes to uncertainty in our picks. We pick the peaks by eye and estimate the uncertainty from 95% of the maximum peak amplitude. This allows us to estimate the uncertainty in our p picks and therefore the uncertainty in the corresponding time intercepts, τ.

3.4. Identify Trends in the Picks

[26] The picks from all of the stations are combined in one plot to identify trends in the picks. We assume that picks with p values that show a trend across multiple stations represent refracted or reflected arrivals, and use the apparent slownesses and time intercepts to estimate velocity structure. Often, trends can be identified, but the picture is confused by p picks that are caused by noise (spurious picks) or imperfect near-source correction. To try to remove some of these spurious picks, we filter the picks by the amplitude of the peak. We want picks that are prominent on their own receiver gather, so we only use picks whose peak amplitude at least a certain percentage of the maximum amplitude of the gather. This filter alone would exclude picks that are clearly seen, but do not have sufficient amplitude when compared to the dominant phase of the gather. We include these peaks by screening for peaks that have large amplitude relative to the energy in the set of receiver gathers. The appropriate screening values are set through trial and error with the particular data set.

[27] Once trends are identified in the p pick plot, they are then checked against the corrected travel time data to verify that the picks are not due to large-amplitude arrivals that appear only on a few traces within the receiver gather. Such phases are usually due to imperfect near-source corrections and are ignored in the velocity modeling.

[28] Each p pick trend is assumed to represent a head wave phase or a reflected phase. For relatively simple layered velocity structure beneath the sources, head waves and reflected phases can be identified by the trends in p and τ. In general, the horizontal slowness, p, of a head wave would be invariant with distance, and the p picks for all receiver gathers showing that phase should be the same. The apparent horizontal slowness of the identified phase is simply the mean of the p picks in the trend. Any trends in the corresponding time intercept (τ) picks reflects the structure beneath and between the sources and receivers. If the p pick trend is representative of a wide-angle reflected phase, the horizontal slowness would systematically increase with increasing offset as the reflection becomes asymptotic in the time domain to the slowness of the head wave of the layer above the reflection interface. This p pick trend would be curved and increasing in value as the offset range of the receiver gathers increased, and would show an curved, decreasing trend in the corresponding time intercepts. We do not expect to see reflected phases with any significant amplitude other than possibly *PmP* because of the large offsets involved in the experiments this analysis is designed for. As a result, we describe the analysis technique and discuss various implications for head waves only.

[29] For horizontal layers of constant velocity, both the horizontal slowness p and time intercept τ would be invariant with distance. In the case of layers with constant dip and velocity, p would be distance invariant and represent the inverse of the apparent velocity of the lower layer, while τ would vary with distance in a linear fashion. The slightly more complicated case of a flat-ramp layer (horizontal layers beneath the sources changing to a constant dip beneath the receivers) results in distance invariant p representing the true horizontal slowness of the lower layer and τ that would vary with distance in a linear fashion. A ramp-flat structure (dipping layers beneath the sources changing to horizontal layers beneath the receivers) yields distance invariant p and τ, where p represents the inverse of the apparent velocity of the lower layer and τ would lead to the thickness of the layers above the interface in question.

3.5. Removing the Effects of Near-Receiver Structure

[30] The τ picks reflect the structure beneath the sources, between the sources and receivers, and beneath the receivers. Since most of the path of a head wave is identical for all receivers recording the particular phase, the variations in τ picks between receiver gathers represent the differences in crustal structure for the corresponding upgoing paths to the receivers. To model this crustal structure, we have to separate broad-scale structure from near-receiver upper-crustal structure, which we will then correct for.

[31] Assuming the broad-scale structure can be parameterized as a layered velocity structure, the τ picks can be fit by a straight line, and a least squares linear fit is applied to the τ picks for each phase. Any variation in the τ picks away from a linear trend are modeled as station delays that are assumed to originate near the receivers. The station delay for each receiver is the average of the deviations for all the phases picked at that receiver. The station delays are removed from the picks and a straight line is fit to each phase. The small remaining residuals are assumed to be due to minor differences in the ray paths for the various phases in the upper crust and errors in picking.

[32] The τ deviations for most picks are much smaller after removing the average station delays. Picks from a receiver gather with large uncertainties in the station delays are not used to calculate the new straight line fits. Large uncertainties indicate stations with bad picks, local complexities in the upper crust, or three-dimensional effects that cannot be modeled with our analysis.

3.6. Velocity Model Suite

[33] Although we have constraints that limit the velocity model, a range of possible models will satisfy the data. We explore the end-member structural models that define the range of possible models. Velocity models with structure intermediate to the end-members will also satisfy the pick data to the same degree.

[34] The p and τ picks provide three sets of constraints for every head wave phase to be used in construction of the velocity model. The first constraint is the apparent horizontal slowness of the phase, represented by the average p, determined as described above. Second, we use the slope of the τ line, $d\tau/dx$, which reflects the changes in the interface depth between stations along a profile. If there is no change in depth of the interface between stations (i.e., the interface is horizontal), $d\tau/dx$ is zero. A positive value of $d\tau/dx$ indicates the interface dips down toward the direction of increasing source-receiver offset, while a negative value indicates the interface dips up. Our third constraint is the intercept of the τ fit line, $\tau(x = 0)$, which indicates the thickness of the crust above the interface.

[35] We define two types of interfaces as structural end-members: constant dip and flat-ramp interfaces. The constant dip interface model (Figure 4a) is defined by two depth parameters (*d1*, *d2*) that control the dip and absolute depth of the interface, and the velocity (*v*) of the layer beneath the interface. For this model, the velocity is estimated from the apparent horizontal slowness and the slope of the τ line, $d\tau/dx$. The p picks give us either the updip or downdip slowness depending on which direction the rays are traveling relative to the interface dip. The change in τ as a function of offset, $d\tau/dx$, is equal to the difference in updip (p_u) and downdip (p_d) slownesses for that particular interface:

$$\frac{d\tau}{dx} = p_d - p_u \tag{3}$$

Using a small dip approximation, the lower interface slowness becomes

$$p_i = \frac{1}{2}(p_d + p_u) = \frac{1}{2}\left(p_u + \left(\frac{d\tau}{dx} + p_u\right)\right) \tag{4}$$

This approximation is valid for dips of less than 10°, and has percent errors in the range of a few percent (1–3% for reasonable structure, with 5% for pathological cases [*Palmer*, 1986]). For a series of stacked dipping layers, the approximation is still valid, but may slightly overestimate the true layer velocity [*Palmer*, 1986].

[36] The flat-ramp interface model (Figure 4b) is defined by three parameters (*d1*, *d2*, *k*) that control the depth of the flat, and the dip and location of the ramp. As long as the interface is flat beneath the downgoing paths of the sources, the apparent horizontal slowness measured for the phase is actually the true slowness (or $1/v$) for the layer beneath the interface. Gaps in the receiver coverage allow a range of flat-ramp interface models, with kink locations between near and far offset limits. These two models (near-offset kink and far-offset kink) show the range in the location of the change in slope of the interface (i.e., the kink, *k*), as constrained by the data. The near-offset kink interface model is limited by the assumption that the arrival from that interface is a straight line in the time domain (i.e., same slope at all offsets). This means the interface cannot slope down from the horizontal before the down-going ray from the last source reaches the interface. The far-offset kink is limited by the assumption of a single linear fit to the τ data for the phase in question (unless the τ trend suggests otherwise). This means that the kink in the interface must occur at or before the upgoing path to the nearest offset receiver leaves the interface. When it is reasonable to fit two separate $d\tau/dx$ slopes to the τ pick data, the kink could be located at a farther offset such that the τ picks show a kink (station kink end-member).

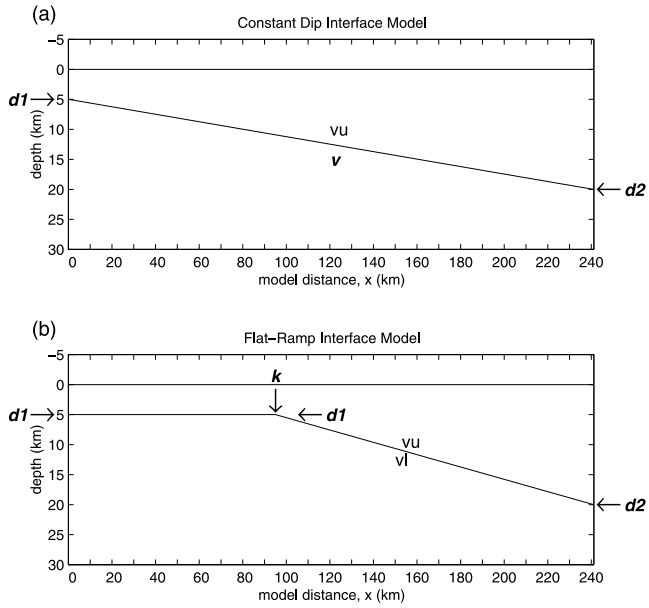

Figure 4. Two types of interface models are defined as structural end-members. (a) Constant dip interface model. Interface depth at left (south) side of model, *d1*. Depth at right (north) side of model, *d2*. Lower layer velocity, *v*. Upper layer velocity, *vu* is fixed in the modeling process. (b) Flat-ramp interface model. Depth of flat portion of interface and depth of interface at left (south) side of model, *d1*. Interface depth at right (north) side of model, *d2*. Location of kink, *k*, marks the transition from flat to dipping interface. Upper and lower layer velocities, *vu* and *vl* respectively, are fixed in the modeling process. Lower layer velocity is the inverse of the horizontal slowness of the phase, $vl = 1/p$.

[37] When constructing our velocity model, we consider each interface individually, to determine the range of possible interface models that fit the data constraints. However, to reach deeper interfaces, the rays travel through all interfaces located above. We must consider all possible configurations for the shallower interfaces when modeling deeper interfaces, creating a model tree.

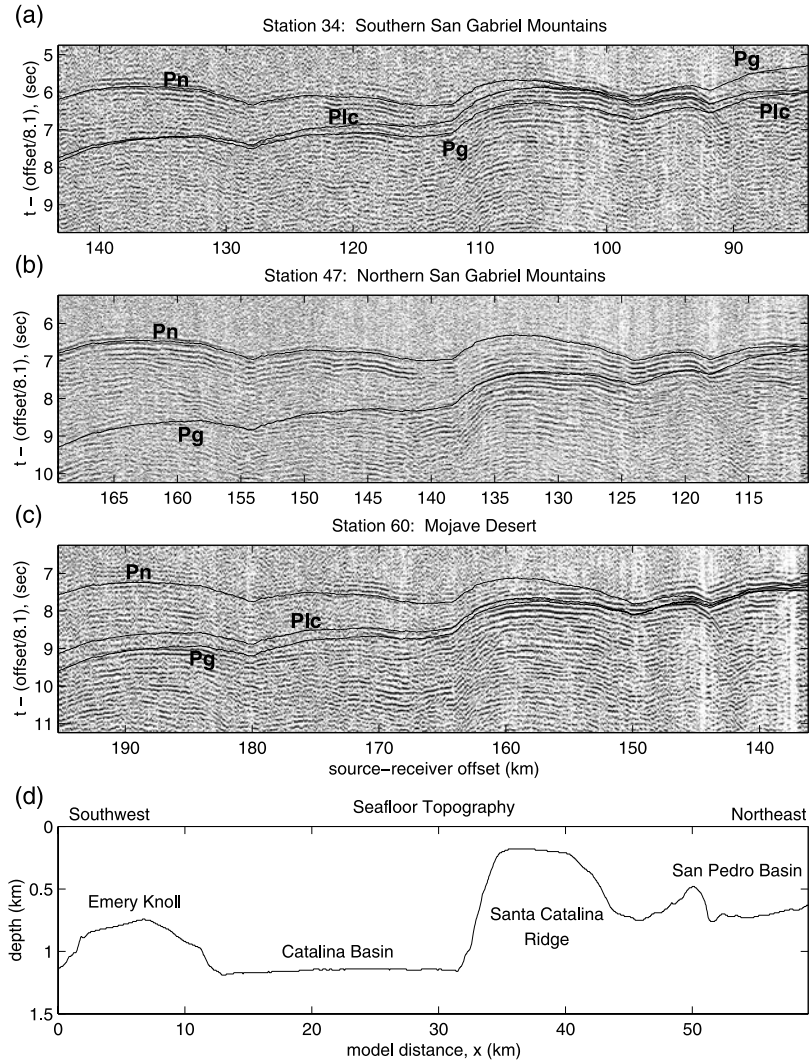

Figure 5. (a–c) Three receiver gathers at different offset ranges showing the same shape lateral time variations and the convergence of secondary arrivals in the nearest half of the offset range. Plotted in reduced time. Phases identified during the analysis are marked approximately by thin lines. Pn, upper mantle head wave; Plc, lower crust head wave; Pg-middle crust head wave. (d) Seafloor topography beneath the ship track. Note there is greater than 1 km of relief in the seafloor.

[38] Using the forward ray tracing program XTRAMP [*Zelt and Smith*, 1992], we find the combination of parameters *d1*, *d2*, and *v* or *k*, that produce the lowest interface model error for the interface in question. We define interface model error as

$$E = \sqrt{\left(\frac{1}{(N-1)}\right)\sum_{i=1}^{N}(\tau_i - T_i)^2} \qquad (5)$$

where τ_i is the corrected time intercept pick of the *i*th station, T_i is the calculated time intercept to the *i*th station from ray tracing, and N is the number of stations with τ picks for the phase in question. This error looks at the misfit of only the model interface in question, regardless of how many other interfaces the rays must traverse to reach this interface. We constrain our search by only considering interface models that produce within the uncertainties, the p, $d\tau/dx$, and $\tau(x = 0)$, measured for the phase being considered.

4. LARSE Data Processing

[39] The varied environments of the receivers (coast, sedimentary basins, mountains, and desert), and significant cultural noise along large sections of the profile, produced widely varying noise contents in the data from the various sources. This required filters to be designed for each receiver. In general, a band pass between 5 and 21 Hz was used. For approximately one-half of the receivers, the upper frequency limit was reduced to 12 Hz to diminish cultural noise. Spiking deconvolution was used to reduce some of the ringing that is prominent in the raw data.

[40] The filtered data clearly show large lateral travel time variations across individual receiver gathers that appear to be common to all receiver gathers (regardless of offset) and the two major phases, *Pn* and *Pg* (Figures 5a–5c). These

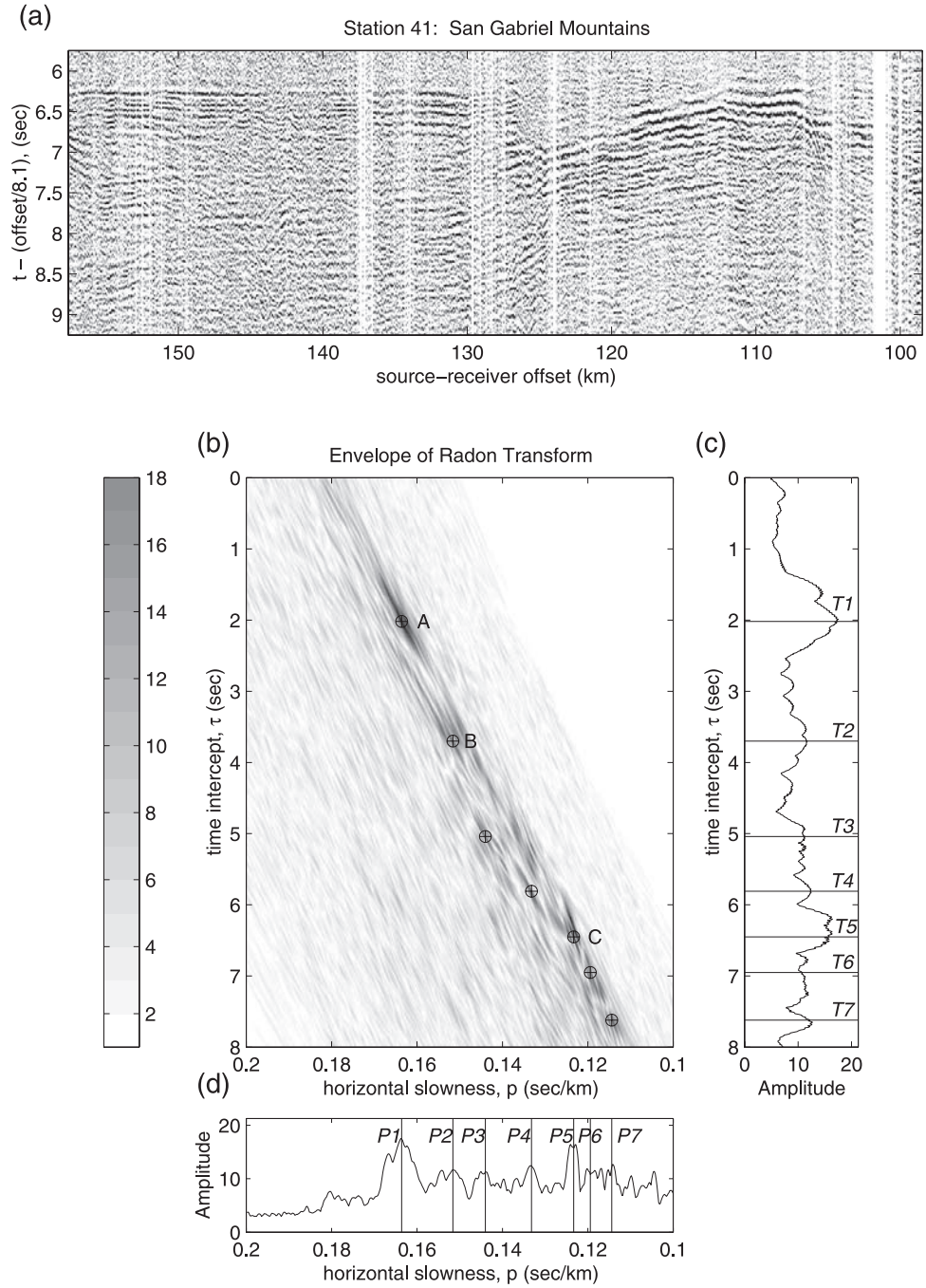

Figure 6. Picking process demonstrated on station 41 data. (a) Reduced time section for station 41 (model distance x = 157.6 km), located in the San Gabriel Mountains. Data have been band-pass filtered, deconvolved, and corrected for near-source effects. (b) Envelope of the Radon transform of the data. Picks 1–7 are marked by a circle surrounding a cross. Picks corresponding to phases A, B, and C are labeled. (c) Maximum amplitude of each row (τ). The seven τ picks shown (T1–T7) correspond to the seven p picks of Figure 4d (P1–P7 respectively). (d) Maximum amplitude of each column (p). Seven p picks correspond to τ picks in 4c.

time variations are due to the near-source effects of the seafloor topography and microbasin structure. Seafloor relief of up to 1 km (Figure 5d) accounts much of this variation, but microbasin structure in the offshore is also a major effect, as is clearly shown in the constant offset section for a parallel ship track in the LARSE multichannel seismic data report [*Brocher et al.*, 1995, Figure 7]. The seafloor topography and the offshore microbasin structure appear to contribute equally to the lateral time variations, so a simple water column correction is inadequate. Therefore we remove the near-source effects empirically. We use *Pn* as the pilot head wave (from station 47; offsets $\sim$ 110–169 km) for the empirical correction because it is the strongest arrival at nearly all offsets and the first arrival at most of the offsets.

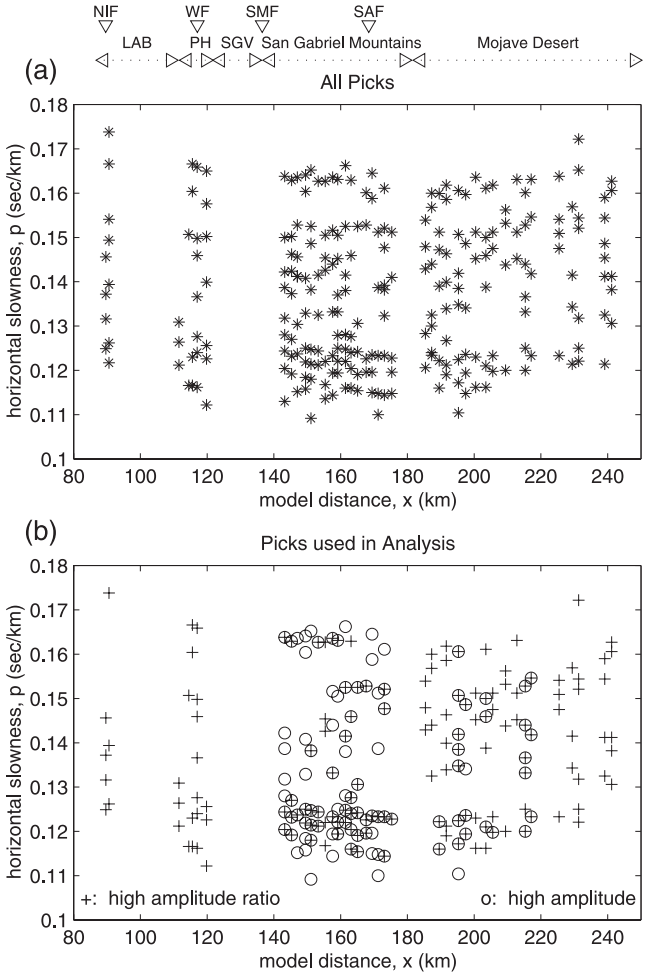

Figure 7. (a) The 251 p picks from all stations, plotted against the model distance, of each station. (b) The 187 "good" p picks. Picks with high-amplitude ratio (at least 70% of the maximum amplitude of the Radon transform envelope) plotted as crosses. Picks with high amplitudes (relative to the energy in the set of receiver gathers) plotted as circles. Some peaks have both high pick amplitude and high-amplitude ratio. Geography and faults are labeled to show location of stations. LAB, Los Angeles Basin; NIF, Newport-Ingelwood Fault; PH, Puente Hills; SAF, San Andreas Fault; SGV, San Gabriel Valley; SMF, Sierra Madre Fault; WF, Whittier Fault.

Approximately 12% of the traces were eliminated because of bad waveforms, apparent cycle skips, and noise.

[41] Figures 6a–6d shows the time section, radon transform envelope, and the corresponding column and row maximum curves for a station located in the San Gabriel Mountains. The solid lines in Figures 6c and 6d indicate the picked peaks for this station. Unlike the synthetic section in Figure 3, the radon transform envelope in Figure 6b has energy distributed away from a single curve due to coherent noise in the time section. This noise contributes to uncertainty in our picks of the peaks and can cause spurious peaks (and thus spurious picks). As a result, average 95% peak uncertainties are 0.001 s/km for p, and 0.16 s for τ. In addition, we estimate the peak amplitude within the wave train reverberations to be delayed approximately 0.25 s for this data set and thus decrease the value of all τ picks by this amount during velocity modeling.

[42] Figure 7a shows all 251 initial p picks for all the stations, as a function of the nearest source-receiver offset. Some trends can be identified, but the picture is confused by picks that are caused by noise or imperfect near-source correction. We filter the picks by only using picks with amplitudes at least 70% of the maximum amplitude of the radon transform envelope or with peak amplitude of at least 10 (Figure 7b). The latter filter allows picks with amplitudes that are small relative to the dominant *Pn* phase but have high amplitudes relative to the energy in the receiver gather set. The amplitude filtering leaves us with 187 picks. Note that trends with consistent p values of $\sim$0.1630 s/km, and $\sim$0.1230 s/km, are now obvious. Trends at p values of $\sim$0.1520 s/km, and $\sim$0.1190 s/km are less obvious. The first three trends can be identified in the corrected travel time data. The fourth trend ($\sim$0.1190 s/km) appears to be due to an imperfect near-source correction, so a small section of high-amplitude traces are slightly out of alignment with the rest of the arrival, and thus appear to have a different slowness and time intercept. This trend is therefore ignored.

5. Results

5.1. Picks and Station Delays

[43] The three p pick trends identified in Figure 7b are shown separated from the other picks in Figures 8a–8c with their corresponding τ picks shown in Figures 9a–9c. We identify the $\sim$0.1230 s/km trend (Phase C) as *Pn*, the $\sim$0.1630 s/km trend (Phase A) as *Pg*, and the $\sim$0.1520 s/km (Phase B) trend as a lower crustal head wave. A least squares linear fit is applied to the τ picks for each phase. Any

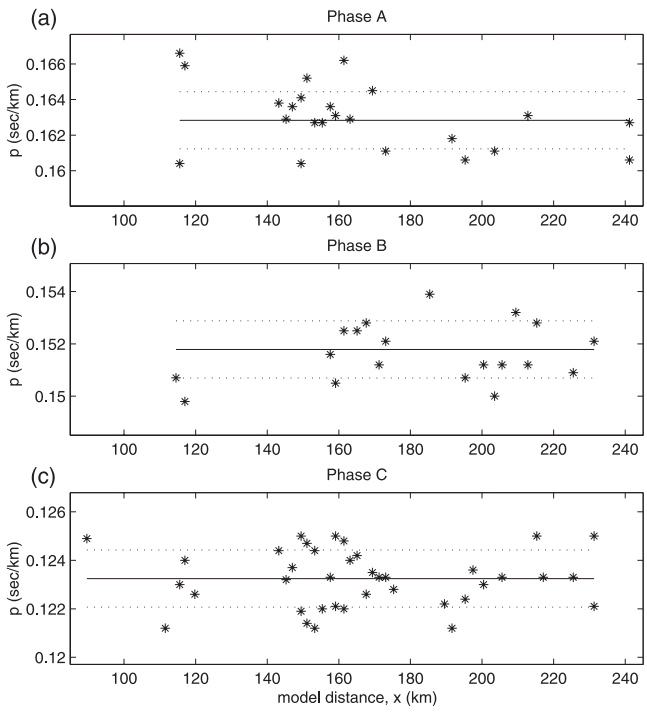

Figure 8. Horizontal slowness (p) picks for the three phases identified. Mean p of each phase marked by solid line with the uncertainty shown as dotted lines.

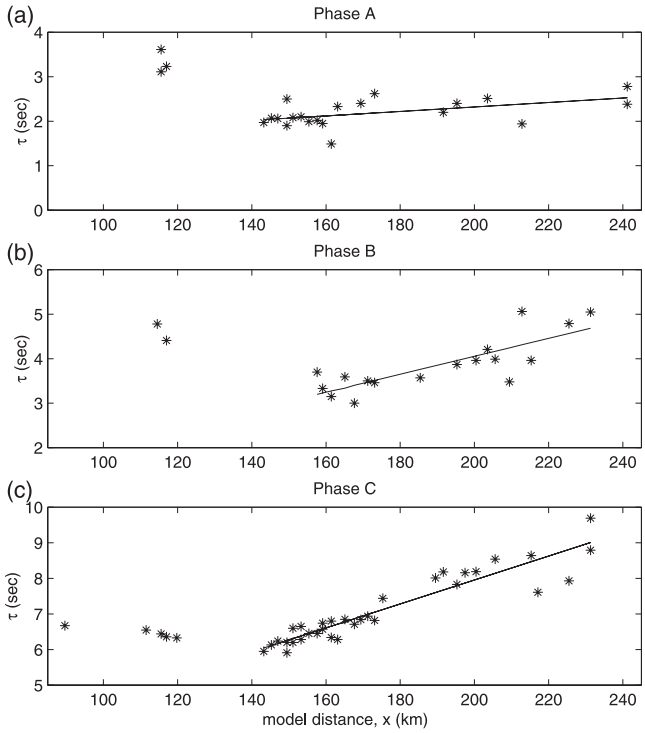

Figure 9. Time intercept (τ) picks for the three phases identified. Solid lines marks the best fit line for the San Gabriel Mountain and Mojave Desert stations ($x > 140$ km). Coastal and basin stations are not used because of the inconsistent delays between different phases.

variation in the τ picks away from a linear trend are modeled as station delays that are assumed to originate near the receivers. The best fit line is calculated for stations in the San Gabriel Mountains and Mojave Desert (model distance, $x > 140$ km). We do not use the coastal and basin stations in the fit because the varying thickness of very slow sediments of the Los Angeles Basin in the upper crust produces delays that cannot be approximated by a simple static shift and would require a more detailed knowledge of the basin structure to use.

[44] Figure 10 shows the average stations delays and the estimated elevation statics for line 1. The smallest uncertainties in general occur for stations in the San Gabriel Mountains. Uncertainties for the Mojave Desert stations (model distance, $x > 180$ km) are the largest in general. Coastal and basin stations (model distance, $x < 120$ km) have smaller formal uncertainties than the Mojave Desert stations because most of these stations have only one phase picked per station. However, these stations contain the largest informal uncertainty because with the large data gaps created by poor quality and non-functioning stations in the Los Angeles Basin and San Gabriel Valley, it is not clear how these stations fit into the structural trends suggested by the τ picks of the San Gabriel Mountains and Mojave Desert stations.

[45] The largest station delays are found in the basin and coastal stations. These delays decrease to the north indicating that the rays are traveling through a thinner sediment column. This is expected, as the northernmost two stations are located in the Puente Hills, north of the Los Angeles structural basin. Coastal stations would lie on the southwestern edge of the Los Angeles basin and would be expected to have smaller delays because the rays would be presumably traveling only part of their up paths through the Los Angeles basin. Relative station delays for the San Gabriel Mountains are within ±0.25 s. Surprisingly, the delays show no correlation with receiver topography.

[46] Figures 11a–11c shows the time intercepts after removing the average station delays, and the single line slope fits to the new τ values. The τ deviations for most picks are much smaller after removing the average station

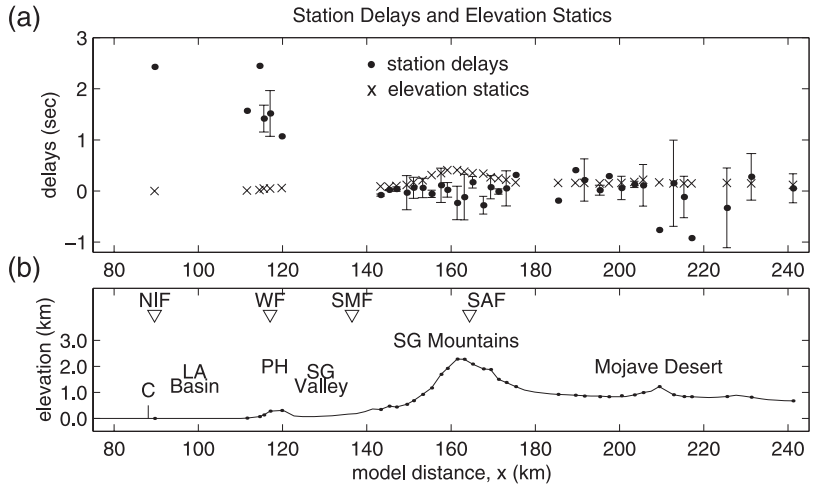

Figure 10. Station delays and elevation statics. (a) Solid circles represent average station delays, with error bars at stations with more than one phase picked. Estimated elevation statics are marked with a cross. Note the lack of correlation of elevation statics and station delays for the San Gabriel Mountains ($140 < x < 180$ km), where some of the stations at the highest elevations have the largest negative delays. (b) Topography. Dots on surface represent receivers. C, coast; LA Basin, Los Angeles Basin; NIF, Newport-Inglewood Fault; PH, Puente Hills; SAF, San Andreas Fault; SG Mountains, San Gabriel Mountains; SG Valley, San Gabriel Valley; SMF, Sierra Madre Fault; WF, Whittier Fault.

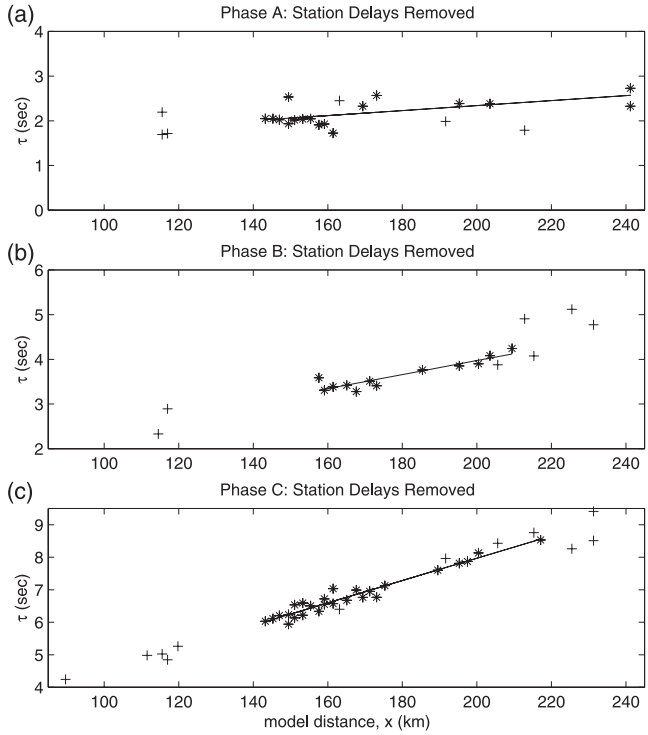

Figure 11. Time intercepts after station delays are removed for the three identified phases. Solid lines marks the best fit line for the San Gabriel Mountain and Mojave Desert stations (x > 140 km). Receivers with large uncertainties in average station delay (>0.40 s) are not used in the fit and are marked by crosses.

delays. Picks with uncertainties in the station delays greater than 0.4 s are not used to calculate the new straight line fits (plotted as crosses, Figures 11a–11c). Large uncertainties indicate stations with bad picks, local complexities in the upper crust, or three-dimensional effects that cannot be modeled with our analysis. As we are interested in the overall broad-scale structure of the region, the loss of a few stations is not important.

5.2. Exploring the Model Space

[47] Although we have constraints that limit the velocity model, a range of possible models will satisfy the data. We explore the end-member structural models that define the range of possible models. Presumably, velocity models with structure intermediate to the end-members will also satisfy the pick data to the same degree.

[48] The wide-angle nature of the experiment precludes information on the upper crust, so we assume a velocity of 5.5 km/s, consistent with the upper crust of the average southern California velocity model [*Wald et al.*, 1995]. Near-surface velocity anomalies in the paths of the receivers will be mapped into the station delays. The apparent velocities of phases A, B, and C suggest they represent velocities of the midcrust, lower crust, and upper mantle, respectively. We will henceforth refer to the velocity interfaces separating the upper crust, midcrust, lower crust, and upper mantle as interfaces A, B, and C.

[49] The τ picks suggest three interface configurations are reasonable for modeling phases A and C (constant dip, near-offset kink, and far-offset kink), while the phase B τ picks suggest four possible configurations (constant dip, and near-offset, far-offset, and station kink flat-ramp). In practice however, the constant dip models do not simultaneously fit within our p, $d\tau/dx$, and $\tau(x = 0)$ constraints for interfaces B and C. These models did not work because interface being modeled pinched out at interface above before the interface was shallow enough to match the intercept of the τ fit curve. As a result, the range of full velocity models (contain all three velocity interfaces) that satisfy the data are limited to eighteen. Table 1 lists the model errors for all A, B, and C interface models for comparison.

5.3. Composite Velocity Model

[50] The composite velocity structure of Figure 12 shows the crustal structure across the transition zone between the thin crust of the Inner California Borderland and the thicker crust onshore. The shaded region surrounding the interface C end-members outlines the region of crust where the Moho is located. Not every interface within this region will satisfy the constraints because the data results from a combination of parameters. For example, an interface following the shallow edge of the shaded region will not satisfy the constraints because the depth of the flat portion of the interface (*d1*) deepens as the location of the kink (*k*) moves northward.

[51] The upper crust (above interface A) thickens gradually northward. In the Borderland, the top of the midcrust occurs at 6.5–8.5 km depth for the flat-ramp models and 4–7 km for the constant dip model. This depth range is similar to the result of *ten Brink et al.* [2000], even though the authors assumed the upper crust to be a steep velocity gradient. Similarly, the velocity model of *Godfrey et al.* [2002] reaches 6.0 km/s at a depth of 8 km in the Borderland. Our estimate of depth to the top of the midcrustal layer beneath the Mojave Desert is much closer to the average 15 km of the 6.3 km/s contour of *Hauksson* [2000], than to the average 5 km depth of the 6.0 km/s contour from the same model. As our midcrustal velocity is intermediate (~6.15 km/s) to the velocity range of this thick moderate velocity section, the discrepancy is likely much smaller than it appears.

[52] Located between interfaces A and B, the thickness of the midcrust in most of our velocity models is 6–10 km beneath the Borderland, but can be as thin as 3 km. The midcrust thickens abruptly beneath the Los Angeles Basin with interface B dips of 18–28°. This transition occurs somewhere between the coastline and the San Gabriel Valley. Both *Hauksson* [2000] and *Godfrey et al.* [2002] show a similar midcrustal thickness beneath the Borderland region. In addition, *Hauksson* [2000] shows a similar increase in depth to the top of the lower crust, deepening from nearly horizontal beneath the Los Angeles Basin, to greater than 25 km at the Sierra Madre Fault.

[53] The lower crust beneath the Borderland is much thinner than that of the average southern California crust (16 km [*Wald et al.*, 1995]). The thickness of the lower crust ranges from 2 to 12 km, averaging 4.4 km for near-offset kink end-members, and 8.3 km for far-offset kink end-members. The velocity of our lower crust is similar to *Godfrey et al.* [2002] and *Hauksson* [2000], although our estimate of the velocity is more robust as it is constrained by the lower crust head wave (phase B). Our data constrain the

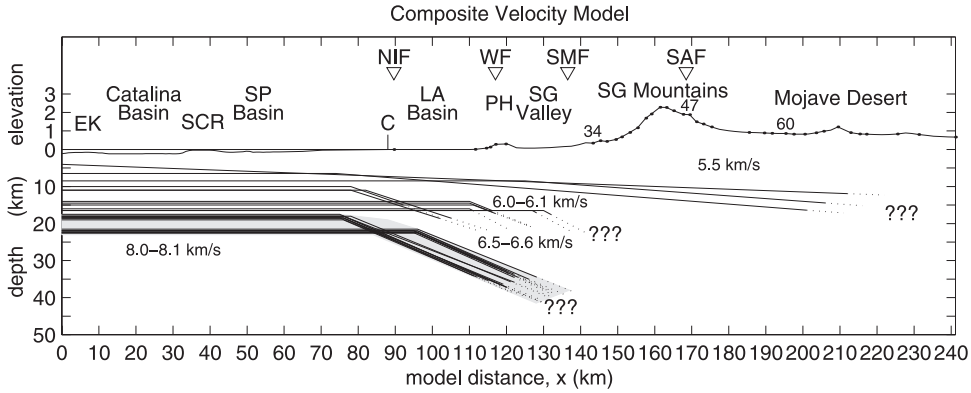

Figure 12. Composite velocity model. Composed of 18 end-member interfaces with reasonable model errors. Surface topography exaggerated 5×. Seafloor topography not exaggerated. Dots represent receivers used in the velocity modeling for interface C. Interface A, B, and C end-members are represented by medium gray, light gray, and black lines, respectively. Question marks indicate the extent of ray coverage for the three interfaces. Shaded region outlines the region of crust where the Moho is located. The velocities are constant for the entire layer within each velocity model. The range of velocities listed for each layer indicates the velocities found in the 18 velocity models plotted. Dots on surface represent receivers. The locations of stations 34, 47, and 60 are identified. C, coast; EK, Emery Knoll; LA Basin, Los Angeles Basin; NIF, Newport-Inglewood Fault; PH, Puente Hills; SAF, San Andreas Fault; SCR, Santa Catalina Ridge; SG Mountains, San Gabriel Mountains; SG Valley, San Gabriel Valley; SMF, Sierra Madre Fault; SP Basin, San Pedro Basin; WF, Whittier Fault.

Moho (interface C) to deepen abruptly, dramatically increasing the vertical thickness of the lower crust as the Moho dips northward 21°–25°. The transition from horizontal to dipping occurs between the shallow offshore slope and the Los Angeles Basin. This range of possible locations is 21 km wide. Our upper mantle velocity of 8.15 km/s is faster than *Godfrey et al.* [2002].

[54] Although our velocity model is similar to that of *Godfrey et al.* [2002], it differs in key aspects that are due to differences in the identification of arrivals (*Pn*, *PmP*, and the lower crust head wave, phase B) and the emphasis of certain phases during forward velocity modeling. In the velocity model of *Godfrey et al.* [2002], the velocity of the lower crust and structure of the Moho beneath the Inner Borderland depends heavily on the arrival identified as *PmP* by the authors. The large lateral time variations due to the seafloor topography and basin structure and the reverberative nature of the wave train complicate the identification of individual arrivals in the time section when they are not the first arrival. This is especially true in the nearest half of the offset range because of the convergence of secondary arrivals. *Godfrey et al.* [2002] identify *PmP* only on the near half of the offset range of their stations (21, 39, 47, 64; their Figure 2) with *Pn* continuing in line on the far half of the offset range. The authors do not pick nor identify the *Pn* arrival on the near half of the offset range, although it should be in front of *PmP* at these offsets (*PmP* becomes critical at offset ~50 km). Interestingly, the changeover from *Pn* to their *PmP* occurs at the southern edge of the Catalina Ridge (a place of large diffractions in the time data). In addition, the largest-amplitude arrivals coincide with the shots above the Catalina Ridge and do not shift with offset as we would expect for a critical angle phenomenon.

[55] We trace *Pn* across nearly the entire offset range in the travel time plots for most of the stations. *PmP* is one of the strong secondary arrivals that converge and overlap in the near half offset range of the time sections, and thus difficult to separate from the other arrivals because of the large lateral travel time variations due to the near-source upper crustal structure. We believe that our identification of *Pn* is correct and due to our analysis technique, we are able to identify an additional phase (phase B, lower crust head wave) which allows us to better constrain the velocities in the mid to lower crust of the Inner Borderland.

6. Discussion

6.1. Station Delays

[56] Station delays for the San Gabriel Mountains show no correlation with receiver topography. While negative station delays and high upper crustal velocities have been previously noted for the San Gabriel Mountains [e.g., *Malin et al.*, 1981; *Hauksson and Haase*, 1997; *Pellerin and Christensen*, 1998], station delays have not been analyzed for relative differences along a profile perpendicular to the strike of the range. With a velocity of 5.5 km/s, one would expect the difference in station delay between the Sierra Madre fault (station 30, no pick data) and the highest station (station 43) to be at least 0.38 seconds s just due to topography alone. This suggests that high-velocity material is located in the shallow upper crust beneath the mountains, such that the effect of additional ray path length to receiver is negated. Not only must high-velocity material exist in the upper crust, it must also have velocities that are proportional to elevation. Higher velocities in the higher core of the range are reasonable if the middle of the range was uplifted and eroded faster than the flanks. The earthquake tomography study by *Hauksson* [2000] supports this interpretation, where cross section (d) in that paper shows velocities of 5.5–6.0 km/s at the surface in the central, topographically high part of the San Gabriel Mountains, decreasing to 4.5–5.5 km/s at lower elevations on either side.

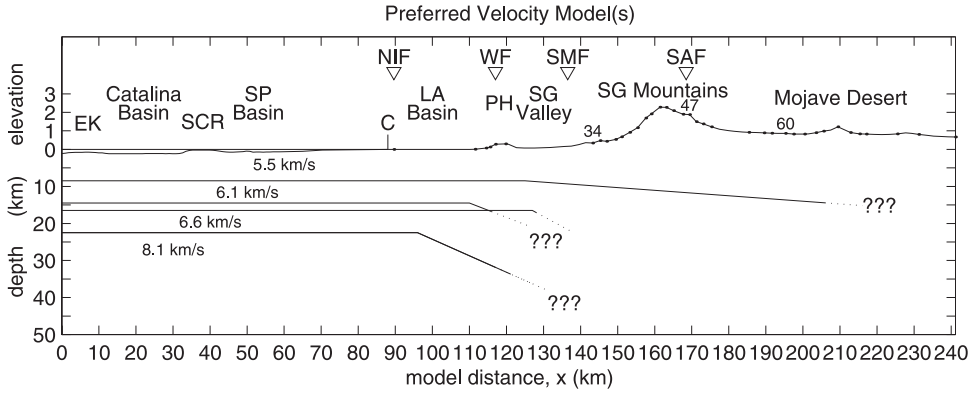

Figure 13. Preferred velocity model. Model is actually composite of two end-member velocity models (205, 208) that contain the same interface A model (model 2), the far-offset and station-kink models for interface B (22, 23), and two interface C models that are identical despite the differences in middle to lower crustal structure. Surface topography exaggerated 5×. Seafloor topography not exaggerated. Dots on surface represent receivers. The locations of stations 34, 47, and 60 are identified. C, coast; EK, Emery Knoll; LA Basin, Los Angeles Basin; NIF, Newport-Inglewood Fault; PH, Puente Hills; SAF, San Andreas Fault; SCR, Santa Catalina Ridge; SG Mountains, San Gabriel Mountains; SG Valley, San Gabriel Valley; SMF, Sierra Madre Fault; SP Basin, San Pedro Basin; WF, Whittier Fault.

[57] The receiver located near the coast has station delays comparable to those located in the Los Angeles Basin proper. This suggests that a comparable amount of slow material may exist in the upper crust offshore of the Seal Beach coast. *Hauksson* [2000] shows slow velocities in the upper 4 km of the crust extending the Los Angeles Basin up to 7 km offshore (cross section d, that paper).

6.2. Location and Width of the Transition Zone

[58] Our analysis shows that we can narrow the range of possible locations of the transition zone by making an assumption about the thickness of the crust in the Inner Borderland. We find that the location of the kink, *k*, in the flat-ramp models is linearly related to the depth of the flat, *d1*. The farther south the kink is located, the shallower the flat portion of the interface. Thus a thinner Borderland crust implies a transition zone further south, while a thicker Borderland crust moves the zone northward.

[59] If we assume that the Moho depth is approximately 22 km in the Inner Borderland as modeled by other recent studies [*Zhu and Kanamori*, 2000; *Hauksson*, 2000; *Godfrey et al.*, 2002], the far-offset kink end-member models represent the location of the initiation of Moho dip. The far-offset kink end-members place the dip initiation at 95–96 km, and hence beneath the southwestern Los Angeles Basin. The ray coverage from our data set allows us to trace this interface to 32–34 km depth (far-offset kink models only) beneath the southern edge of the San Gabriel Valley. This means that the transition zone from thin Inner Borderland crust (~22 km) to average southern California crust (~32 km) occurs over a horizontal distance of approximately 20–25 km.

[60] *Hauksson* [2000] used the distribution of *P* wave velocity in the lower crust to constrain the width of the transition zone to be 30–80 km wide in a region containing the Los Angeles Basin. Our results provide a more precise location and width of the transition zone. The width of the transition zone in the Inner California Borderland is similar to that of other locations along the central California coast, where the crust thickens over a distance of 20–30 km (between the Hosgri fault and the coastline), and not 60–80 km as previously cited [*Fuis*, 1998].

6.3. Velocity Model

[61] Although our study shows that a range of models satisfy the data constraints, we present our ''preferred model(s)'' in Figure 13. This model is a composite of two end-member velocity models (models 205, 208) that contain the same interface A model (2), the far-offset and station-kink models for interface B (models 22, 23), and two interface C models that are identical despite the differences in middle to lower crustal structure. Model 2 was chosen for interface A to agree with the thickness of the upper crust beneath the Inner Borderland from recent southern California velocity models [e.g., *Hauksson*, 2000; *ten Brink et al.*, 2000; *Godfrey et al.*, 2002]. We chose models 22 and 23 for interface B because we believe it is more reasonable for the lower crust to follow the Moho and initiate the abrupt midcrustal thickening to the north of that of the Moho. The models for interface C followed from the lower interface models, with the assumption that the thickness of the crust beneath the Inner Borderland is 22 km.

[62] The Borderland is believed to have an oceanic origin [*Mooney and Weaver*, 1989] but has a thicker crust than normal oceanic crust. Most of the additional thickness is contained within the upper and middle crust. The lower crust has a velocity (6.6 km/s) consistent with layer 3 of normal oceanic crustal structure (vp = 6.73 ± 0.19 km/s [*Christensen and Salisbury*, 1975]), but the thickness of 6–8 km may or may not be consistent, depending on the location of the kink in phase B (i.e., average thickness = 4.97 ± 1.25 km [*Christensen and Salisbury*, 1975]). *Ten Brink et al.* [2000] find no evidence for velocities greater than 6.5 km/s in the Borderland beneath line 1, except for a limited high-velocity ridge. This may result from the limited offset range (<60 km) of the OBS data used in their study.

[63] Although our modeled upper mantle velocity is faster than average southern California upper mantle (7.8 km/s

[*Wald et al.*, 1995]), most of the upper mantle in our velocity model is beneath the Inner Borderland, a region whose deeper structure is not well known because of the lack of studies with adequate coverage at depth. Earthquake source tomographic studies are limited by sparse ray coverage in the offshore, especially at depth [*Hearn and Clayton*, 1986; *Sung and Jackson*, 1992; *Hauksson and Haase*, 1997; *Hauksson*, 2000]. The previous crustal seismic refraction study conducted in the Inner California Borderland [*Shor and Raitt*, 1958] found a velocity of 8.2 km/s at a depth of 24 km beneath the Catalina Basin (Figure 1). *Christensen and Salisbury* [1975] find upper mantle velocities of 8.15 ± 0.31 km/s beneath normal oceanic crust older than 15 m.y. Inland of the crustal transition zone, upper mantle velocities should revert to the well established southern California average of 7.8 km/s [*Wald et al.*, 1995].

[64] The Inner California Borderland seems to be modified and thickened oceanic crust, with the oceanic upper mantle intact beneath it. *Pn* is a strong, coherent, and continuous phase that is seen across the entire profile to source-receiver offsets of over 230 km. Although we do not model the relative amplitudes of *Pn* and the other arrivals, qualitatively, the strength and continuity of the *Pn* phase with increasing offset can be viewed in the receiver gathers. This suggests the Moho (interface C) must be coherent and laterally continuous with only long wavelength variations, because short wavelength variations would diffract and attenuate the head wave phase energy. There is no reason to believe that the rest of the oceanic lithosphere beneath the upper mantle is absent. This suggests that a stalled fragment of subducted oceanic lithosphere remains beneath the Inner California Borderland.

[65] During the late Oligocene, when the Pacific-Farallon spreading center was approaching the Farallon-North American trench, the subducting slab was very young and quite buoyant. The Farallon slab was breaking into fragments as it approached the trench. The young crust would have positive buoyancy relative to the underlying mantle, and if there were no slab pull to drag it beneath the continent, it could easily plate to the underside of the continent near the trench [*Bohannon and Parsons*, 1995]. While young slabs reheat at sublithospheric levels, young crust at shallow levels cools and strengthens rather than sinking [*Bohannon and Parsons*, 1995]. If a break occurred in the subducted slab inland from the trench, the fragments would remain underpinned to the continent and any slab gap would form inland from the trench, or occur at a deep enough level that it has little effect on the continental lithosphere above the slab gap [*Bohannon and Parsons*, 1995].

[66] This fragment may be the southern portion of the partially subducted Monterey microplate imaged to the north, or a fragment of the north dipping Arguello microplate possibly seen south of the Morro fracture zone [*Nicholson et al.*, 1992, 1994]. *Atwater and Stock* [1998] state that the Monterey microplate could extend further beneath southern California because their modeling only showed the minimum area of the fragment. The close proximity to the Transverse Ranges and the northward dip makes this material a prime candidate for the postulated oceanic lithosphere that is descending into the mantle beneath the Transverse Ranges [*Bird and Rosenstock*, 1984; *Humphreys*, 1995; *Atwater and Stock*, 1998].

Table 1. Composite Velocity Model Interfaces[a]

Interface Model	Type	*d*1, km	*d*2, km	*k*, km	*v*, km/s	Interface Model Error E, s	Interface A Mode l Used	Interface B Model Used
1	FR	6.5	19.5	74	6.1	0.21		
2	FR	8.5	17.0	125	6.1	0.21		
3	CD	4.0	13.0		6.0	0.22		
11	FR	11.0	63.0	82	6.6	0.12	1	
12	FR	15.0	64.0	111	6.6	0.12	1	
13	FR	16.5	75.0	130	6.6	0.12	1	
21	FR	11.0	63.0	78	6.6	0.13	2	
22	FR	14.5	65.0	110	6.6	0.13	2	
23	FR	16.5	78.0	127	6.6	0.13	2	
31	FR	10.0	67.0	78	6.5	0.12	3	
32	FR	14.0	67.0	110	6.5	0.13	3	
33	FR	16.0	85.0	110	6.5	0.13	3	
101	FR	17.5	90.0	75	8.1	0.16	1	11
102	FR	22.0	87.0	95	8.1	0.16	1	11
104	FR	18.5	87.5	75	8.1	01.6	1	12
105	FR	22.5	87.5	95	8.1	01.6	1	12
107	FR	18.5	92.0	76	8.1	01.6	1	13
108	FR	22.5	88.0	96	8.1	01.6	1	13
201	FR	18.0	90.0	76	8.1	01.6	2	21
202	FR	22.0	87.0	96	8.1	01.6	2	21
204	FR	18.5	87.0	76	8.1	01.6	2	22
205	FR	22.5	87.0	96	8.1	01.6	2	22
207	FR	18.5	90.0	76	8.1	01.6	2	23
208	FR	22.5	87.0	96	8.1	01.6	2	23
301	FR	18.0	85.0	78	8.1	01.7	3	31
302	FR	22.0	85.0	96	8.1	01.6	3	31
304	FR	19.0	90.0	76	8.0	01.6	3	32
305	FR	22.0	85.0	95	8.0	01.6	3	32
307	FR	18.0	82.0	76	8.0	01.6	3	33
308	FR	21.5	80.0	96	8.0	01.6	3	33

[a]Each interface must be considered individually to determine range of possible interface models that fit data constraint. Interface model types: CD for constant dip and FR for flat-ramp. Interface depths at left (south) and right (north) sides of model region, *d*1 and *d*2; *k* is location of kink in flat-ramp models (not a parameter for constant dip models). Lower layer velocity, *v*, is a variable parameter for constant dip interface models but is fixed by the inverse of phase horizontal slowness (1/*p*) for flat-ramp interface models. Interface model error E, as defined in (5). Interface A and B model numbers are used when modeling deeper interfaces.

[67] Many authors have argued against the possibility of remnant oceanic lithosphere beneath the California Borderland (especially the Inner Borderland) citing rifting and extension in the wake of the rotation of the Western Transverse Ranges [*Crouch and Suppe*, 1993; *Nicholson et al.*, 1994] necessary to exhume the high-grade, blueschist facies Catalina Schist from a metamorphism depth of 10–15 km [*Crouch and Suppe*, 1993], "extensive" mid-Miocene volcanism in the Inner Borderland, and high heat flow values in the Inner Borderland and onshore Los Angeles Basin. The above observations seem to require a slab gap to act as a heat source by allowing mantle upwelling to the base of the crust. The schist exhumation seems problematic in light of the continuous and coherent nature of the Moho in the Inner Borderland and the proposed remnant slab fragment. However, the Santa Maria Basin is proposed to have undergone similar rifting and extension to the Inner Borderland [*Crouch and Suppe*, 1993], yet is underlain by the partially subducted Monterey microplate [*Nicholson et al.*, 1992]. Apparently extension and modification in the upper to midcrust can occur without removal of the oceanic slab fragment beneath. The mid-Miocene volcanic rocks of

the Inner Borderland do not necessitate the removal of the slab either because they erupted along the edge of the region of exhumed schist [*Bohannon and Geist*, 1998] and are not distributed throughout as might be expected above a slab gap. The heat source seemingly required by the cited observations may in fact be the young, hot, stalled oceanic slab stalled beneath the margin, rather than the lack of one. *Brocher et al.* [2000] find that such tectonically stalled slabs at the base of the forearc can provide sufficient heat flow from the high temperatures of the oceanic crust itself to explain the volcanism and high heat flow of the Coast Ranges in central California (a region hypothesized to overlie a slab gap, but seismic experiments trace the oceanic slab from the fossil trench to beyond the Coast Ranges). The presence of young, hot fragment of oceanic lithosphere stalled beneath the margin may thus explain the observations used to argue against the possibility of its existence.

7. Conclusions

[68] The results we have presented provide new information on the mid to lower crustal and upper mantle structure in the transition zone from the Inner California Borderland to the on land adjacent continental region. We have created a composite velocity model that constrains the crustal thickness and location and width of the transition zone. The time intercepts of *Pn* require the Moho to deepen significantly to the north. Our velocity model analysis requires the crustal thickness to increase dramatically over a relatively short distance (~20–25 km). The location of the transition zone is constrained to initiate between the offshore slope (~13 km offshore) and the Los Angeles Basin (~8 km onshore). Assuming a crustal thickness of 22 km for the Borderland further constrains the location of the transition zone to be in a 2 km wide region beneath the southwest Los Angeles Basin. The strong, coherent, and continuous *Pn* phase suggests the Moho is coherent and laterally continuous with only long wavelength variations. The Inner California Borderland seems to be modified and thickened oceanic crust, with the oceanic upper mantle intact beneath it.

[69] **Acknowledgments.** We are grateful to Jeanne Hardebeck, Egill Hauksson, and Patricia Persaud for their reviews of an earlier version of this manuscript. Reviews by Robert Hawman, David Okaya, an anonymous reviewer, and the Associate Editor led to a greatly improved manuscript. We thank Collin Zelt for the use of his program XTRAMP. The map was created with GMT software [*Wessel and Smith*, 1991]. This work was supported by the Southern California Earthquake Center, which was funded by NSF Cooperative Agreement EAR-8920136 and USGS Cooperative Agreements 14-08-0001-A0899 and 1434-HQ-97AG01718. SCEC contribution 445. Contribution 8925, Division of Geological and Planetary Sciences, California Institute of Technology, Pasadena.

References

Atwater, T., Plate tectonic history of the northeast Pacific and western North America, in *The Geology of North America*, vol. N, *The Eastern Pacific Ocean and Hawaii*, edited by E. L. Winterer and D. M. Hussong, pp. 21–72, Geol. Soc. of Am., Boulder, Colo., 1989.

Atwater, T., and J. Stock, Pacific-North America plate tectonics of the Neogene southwestern United States—An update, *Int. Geol. Rev.*, *40*, 375–402, 1998.

Bird, P., and R. W. Rosenstock, Kinematics of present crust and mantle flow in southern California, *Geol. Soc. Am. Bull.*, *95*, 946–957, 1984.

Bohannon, R. G., and E. Geist, Upper crustal structure and Neogene tectonic development of the California continental borderland, *Geol. Soc. Am. Bull.*, *110*, 779–800, 1998.

Bohannon, R. G., and T. Parsons, Tectonic implications of post-30 Ma Pacific and North American relative plate motions, *Geol. Soc. Am. Bull.*, *107*, 937–959, 1995.

Brocher, T. M., R. W. Clayton, K. Klitgord, R. Bohannon, R. Sliter, J. McRaney, J. Gardner, and J. Keene, Multichannel seismic-reflection profiling on the R/V Ewing during the Los Angeles Region Seismic Experiment (LARSE), California, *U.S. Geol. Surv. Open File Rep., 95–228*, 1995.

Brocher, T. M., U. S. ten Brink, and T. Abramovitz, Synthesis of crustal seismic structure and implications for the concept of a slab gap beneath coastal California, in *Tectonic Studies of Asia and the Pacific Rim, Int. Book Ser.*, vol. 3, edited by W. G. Ernst and R. G. Coleman, pp. 232–243, Geol. Soc. of Am., Boulder, Colo., 2000.

Christensen, N. I., and M. H. Salisbury, Structure and constitution of the lower oceanic crust, *Rev. Geophys.*, *13*, 57–83, 1975.

Couch, R. W., and R. P. Riddihough, The crustal structure of the western continental margin of North America, in *Geophysical Framework of the Continental United States*, edited by L. C. Pakiser and W. D. Mooney, *Mem.Geol. Soc. Am.*, *172*, 103–128, 1989.

Crouch, J. K., and J. Suppe, Late Cenozoic evolution of the Los Angeles basin and inner California borderland: A model for core complex-like crustal extension, *Geol. Soc. Am. Bull.*, *105*, 1414–1434, 1993.

Ehlig, P. L., Origin and tectonic history of the basement terrane of the San Gabriel Mountains, central Transverse Ranges, in *The Geotectonic Development of California*, vol. 1, edited by W. G. Ernst, pp. 253–283, Prentice-Hall, Englewood, N. J., 1981.

Emery, K., General geology of the offshore area, southern California, *Bull. Calif. Div. Mines Geol.*, *170*, 107–111, 1954.

Fuis, G. S., Western margin of North America—A synthesis of recent seismic transects, *Tectonophysics*, *288*, 265–292, 1998.

Fuis, G., et al., Images of crust beneath southern California will aid study of earthquakes and their effects, *Eos Trans. AGU*, *77*, 173, 176, 1996.

Godfrey, N. J., G. S. Fuis, V. Langenheim, D. A. Okaya, and T. M. Brocher, Lower crustal deformation beneath the central Transverse Ranges, southern California: Results from the Los Angeles Region Seismic Experiment, *J. Geophys. Res.*, *107*(B7), 2144, doi:10.1029/2001JB000354, 2002.

Hauksson, E., Crustal structure and seismicity distribution adjacent to the Pacific and North American plate boundary in southern California, *J. Geophys. Res.*, *105*, 13,875–13,903, 2000.

Hauksson, E., and J. S. Haase, Three-dimensional *Vp* and *Vp*/*Vs* velocity models of the Los Angeles basin and central Transverse Ranges, California, *J. Geophys. Res.*, *102*, 5423–5453, 1997.

Hearn, T. M., and R. W. Clayton, Lateral velocity variations in southern California. II. Results for the lower crust from Pn waves, *Bull. Seismol. Soc. Am.*, *76*, 495–509, 1986.

Humphreys, E. D., Post-Laramide removal of the Farallon slab, western United States, *Geology*, *23*, 987–990, 1995.

Kohler, M. D., and P. M. Davis, Crustal thickness variations in Southern California from Los Angeles Region Seismic Experiment (LARSE) passive phase teleseismic travel times, *Bull. Seismol. Soc. Am.*, *87*, 1330–1344, 1997.

Kohler, M. D., P. M. Davis, H. Liu, M. Benthien, S. Gao, G. Fuis, R. W. Clayton, D. Okaya, and J. Mori, Data report for the 1993 Los Angeles Region Seismic Experiment (LARSE93), southern California: A passive study from Seal Beach northeast through the Mojave Desert, *U.S. Geol. Surv. Open File Rep., 96–85*, 1996.

Luyendyk, B. P., M. J. Kamerling, and R. Terres, Geometric model for Neogene crustal rotations in southern California, *Geol. Soc. Am. Bull.*, *91*, 211–217, 1980.

Malin, P. E., M. H. Gillespie, P. C. Leary, and T. L. Henyey, Crustal structure near Palmdale, California, from borehole-determined ray parameters, *Bull. Seismol. Soc. Am.*, *71*, 783–803, 1981.

Mooney, W. D., and C. S. Weaver, Regional crustal structure and tectonics of the Pacific Coastal States; California, Oregon, and Washington, in *Geophysical Framework of the Continental United States*, edited by L. C. Pakiser and W. D. Mooney, *Geol. So. Am. Mem.*, *172*, pp. 129–162, 1989.

Nicholson, C., C. C. Sorlien, and B. P. Luyendyk, Deep crustal structure and tectonics in the offshore southern Santa Maria Basin, California, *Geology*, *20*, 239–242, 1992.

Nicholson, C., C. C. Sorlien, T. Atwater, J. C. Crowell, and B. P. Luyendyk, Microplate capture, rotation of the western Transverse Ranges, and initiation of the San Andreas transform as a low angle fault system, *Geology*, *22*, 491–495, 1994.

Okaya, D., J. Bhowmik, G. Fuis, J. Murphy, M. Robertson, A. Chakaborty, M. Benthien, K. Hafner, and J. Norris, Report for airgun data acquired at onshore stations during the Los Angeles Region Seismic Experiment (LARSE), California, *U.S. Geol. Surv. Open File., 96–297*, 1996.

Palmer, D., *Refraction Seismics: The Lateral Resolution of Structure and Seismic Velocity*, 269 pp., Geophys. Press, Amsterdam, 1986.

Pellerin, C. L. M., and N. I. Christensen, Interpretation of crustal seismic velocities in the San Gabriel-Mojave region, southern California, *Tectonophysics*, *286*, 253–271, 1998.

Richards-Dinger, K. B., and P. M. Shearer, Estimating crustal thickness in southern California by stacking Pmp arrivals, *J. Geophys. Res.*, *102*, 15,211–15,224, 1997.

Shepard, F. P., and K. O. Emery, Submarine topography off the southern California coast-Canyons and tectonic interpretation, *Geol., Soc. Am. Spec. Pap.*, *31*, 171 pp., 1941.

Shor, G. G., Jr., and R. W. Raitt, Seismic studies in the southern California Continental Borderland, in *Congresso Geologico Internacional*, *XXa Seccion*, *1956, Mexico, Seccion IV, Segundo Tomo*, pp. 243–259, Int. Geol. Congr., Mexico City, 1958.

Sung, L., and D. D. Jackson, Crustal and uppermost mantle structure under southern California, *Bull. Seismol. Soc. Am.*, *82*, 934–961, 1992.

ten Brink, U. S., R. M. Drury, G. K. Miller, T. Brocher, and D. Okaya, Los Angeles Region Seismic Experiment (LARSE), California off-shore seismic refraction data, *U.S. Geol. Surv. Open File Rep., 96–27*, 29 pp., 1996.

ten Brink, U. S., J. Zhang, T. M. Brocher, D. A. Okaya, K. D. Klitgord, and G. S. Fuis, Geophysical evidence for the evolution of the California Inner Continental Borderland as a metamorphic core complex, *J. Geophys. Res.*, *105*, 5835–5857, 2000.

Wald, L. A., L. K. Hutton, and D. D. Given, The Southern California Network Bulletin: 1990–1993 summary, *Seismol. Res. Lett.*, *66*, 9–19, 1995.

Wessel, P., and W. H. F. Smith, Free software helps map and display data, *Eos Trans. AGU*, *72*, 441, 445–446, 1991.

Wright, T. L., Structural geology and tectonic evolution of the Los Angeles basin, California, in *Active Margin Basins*, edited by K. T. Biddle, *Mem. Am. Assoc. Pet. Geol.*, *52*, 35–134, 1991.

Yerkes, R. F., T. H. McCullough, J. E. Schoellhamer, and J. G. Vedder, Geology of the Los Angeles Basin, California—An introduction, *U.S., Geol. Surv. Prof. Pap., 420–A*, 57 pp., 1965.

Yilmaz, O., *Seismic Data Processing*, Soc. of Explor. Geophys., Tulsa, Okla., 1987.

Zelt, C. A., and R. B. Smith, Seismic traveltime inversion for 2-D crustal velocity structure, *Geophys. J. Int.*, *108*, 16–34, 1992.

Zhu, L., and H. Kanamori, Moho depth variations in southern California from teleseismic receiver functions, *J. Geophys. Res.*, *105*, 2969–2980, 2000.

R. W. Clayton and J. J. Nazareth, Seismological Laboratory, California Institute of Technology, Pasadena, CA 91123, USA. (julie@gps.caltech.edu; clay@seismo.gps.caltech.edu)